Science Advances
AAAS

advances.sciencemag.org/cgi/content/full/5/7/eaaw4718/DC1

Supplementary Materials for

Spin fluctuation induced Weyl semimetal state in the paramagnetic phase of $EuCd_2As_2$

J.-Z. Ma, S. M. Nie, C. J. Yi, J. Jandke, T. Shang, M. Y. Yao, M. Naamneh, L. Q. Yan, Y. Sun, A. Chikina, V. N. Strocov, M. Medarde, M. Song, Y.-M. Xiong, G. Xu, W. Wulfhekel, J. Mesot, M. Reticcioli, C. Franchini, C. Mudry, M. Müller, Y. G. Shi*, T. Qian*, H. Ding, M. Shi*

*Corresponding author. Email: ming.shi@psi.ch (M.Sh.); tqian@iphy.ac.cn (T.Q.); ygshi@iphy.ac.cn (Y.G.S.)

Published 12 July 2019, *Sci. Adv.* **5**, eaaw4718 (2019)
DOI: 10.1126/sciadv.aaw4718

This PDF file includes:

Spin splitting and band broadening by static disorder with finite correlation length

Here we analyze in more detail, how quasi-static magnetic fluctuations with different spatial correlations affect the electronic spectrum, going beyond the infinite range correlations discussed in the main text. We treat the magnetic fluctuations arising from the magnetic moments of the Eu 4f orbitals as follows. In the spirit of the Born-Oppenheimer approximation, we model the magnetic fluctuations by a statistical ensemble of random energies $B(x)$, such as Zeeman energies, say, with the Gaussian distribution

$$\overline{B(x)} = 0 \tag{S1a}$$

$$\overline{B(x)B(x')} = B_*^1 e^{-|x-x'|/\xi} \tag{S1b}$$

The disorder thus depends on two parameters, the standard deviation B_* and the correlation length ξ, which is the correlation length below which the microscopic Eu spins are ferromagnetically aligned in three-dimensional space. For simplicity we assume correlations to be isotropic. Note that ξ is bounded from below by the lattice spacing a. As a function of temperature T, ξ reaches a maximum above the antiferromagnetic ordering temperature T_N and reaches the lattice spacing a upon approaching T_N from above, as well as $T \to \infty$. A ferromagnetic alignment of spins introduces a spin splitting of order B_*. In momentum space the dispersion curves are split by Δk_S (denoted W_S in the main text), where

$$\Delta k_S = \frac{B_*}{\hbar v_F} \tag{S1c}$$

For a gas of itinerant electrons for which spin is a good quantum number the Fermi energy ε_F is related to the Fermi wave number k_F and the Fermi velocity v_F through

$$\varepsilon_F = \hbar v_F k_F \tag{S2}$$

For a good metal, $1/k_F$ is of the order of the lattice spacing a.

Perturbing this spin-degenerate electron gas with random static magnetic fields results in the mean-free path l, i.e., the scattering length within the Born approximation. Its dependence on the dimensionless numbers B_*/ε_F and $k_F\,\xi \gg 1$ is

$$l \sim \left(\frac{\varepsilon_F}{B_*}\right)^2 \frac{1}{k_F \xi} \frac{1}{k_F} \tag{S3}$$

(The factor $k_F\,\xi$ that enters the Born scattering time arises from having a multiplicative gain in forward or backward scattering by the number ξ^d of parallel spins in the correlated disordered region, divided by the factor ξ^{d-1} accounting for the fact that scattering is confined to small angles $\sim 1/k_F\xi$. In other words, the problem reduces essentially to 1-dimensional ray optics in the limit $\xi \gg 1/k_F$. For 1d problems the decrease of the mean free path $\sim 1/\xi$ is indeed well established.) According to Eq. (S3), the mean-free path decreases as B_* or ξ increase, as long as the random magnetic energies can be treated perturbatively. If we define the length scale

$$\xi_* \equiv \frac{\hbar v_F}{B_*} \equiv \frac{1}{\Delta k_x} \equiv \frac{1}{W_s} \tag{S4a}$$

we may combine Eqs. (S2) and (S3) into

$$l \sim (\frac{\xi_*}{\xi})\xi_* \tag{S4b}$$

The spin splitting B_* produced by a spatially homogeneous magnetic configuration should be compared to the energy uncertainty $\hbar v_F/\xi$ arising from confining a ballistic electron at the Fermi energy in a box of linear size ξ. The spin splitting becomes only important if

$$B_* \gtrsim \frac{\hbar v_F}{\xi} \tag{S5a}$$

i.e.,

$$\xi \gtrsim \xi_*. \tag{S5b}$$

In the regime

$$a \leq \xi \ll \xi_*, \tag{S6a}$$

the effects of the static random magnetic energies is to give a small uncertainty to the single-particle dispersion of the unperturbed electron gas, i.e., the *k*-dependence of the electronic spectral function is a narrow Lorentzian of width $1/l$ instead of a delta function (see left inset in Fig. S8). No spin splitting can be resolved within this narrow Lorentzian. Indeed, the electronic motion cannot be confined to a correlation volume, and thus averages over the random magnetic field. However, once

$$\xi \sim \xi_*, \tag{S6b}$$

the effect of the static random magnetic energies on the single-particle dispersion of the spin-degenerate electron gas is non-perturbative. The k-dependence of the electronic spectral function still has a broad single peak as a function of k, but with a width of order $1/\xi_* = \Delta k_S$ (see right middle inset in Fig. S8). In the regime

$$\xi \gg \xi_* , \tag{S6c}$$

because the electrons travel in sufficiently large regions in which the magnetic field is uniform, the energy gain B_* resulting from splitting the Kramers' degeneracy in the bulk of these correlated regions is much larger than the energy uncertainty due to scatterings at their (random) boundaries. The k-dependence of the electronic spectral function becomes a double Lorentzian with the two peak maxima separated by $\Delta k_S \equiv W_S$, which is larger than the width $1/\xi$ of either one of the two peaks (see right inset in Fig. S8). Hence, the splitting of the Kramers' degenerate bands now can be resolved. The resolution increases with increasing ξ. In particular, the mean free path is not anymore given by Eq. (S3), but simply tracks ξ. The qualitative dependence on ξ of the mean-free path in the regimes (6a) and (6c) is shown in Fig. S8 assuming that the random magnetic energies can be treated perturbatively around the limiting cases $\xi \to a$ (no spin splitting of the bands) and $\xi \to \infty$ (two spin split bands).

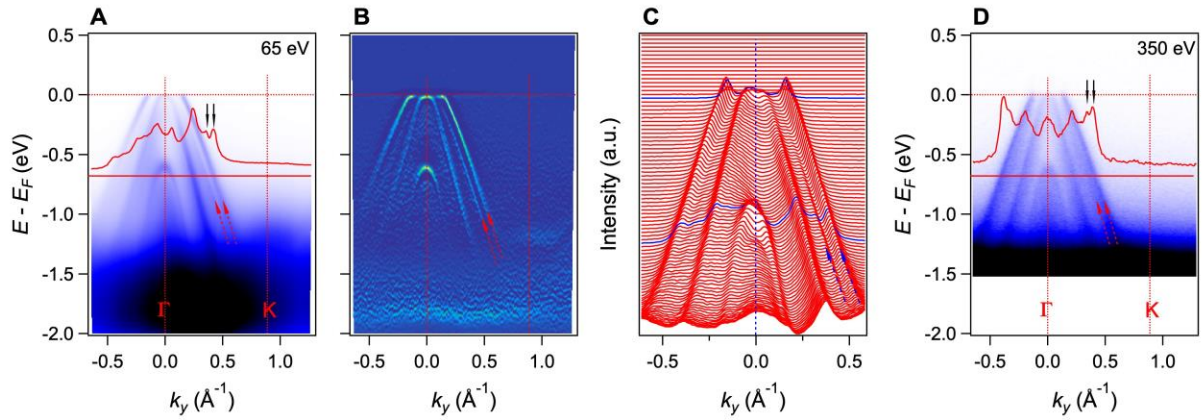

Fig. S1. Band splitting in $EuCd_2Sb_2$. (**A**,**B**) The ARPES spectrum and its curvature intensity plot along Γ-K. The data was collected at 15K with photon energy $h\nu$ = 65 eV. The red arrows indicate the split bands. The red curve in (A) is the momentum distribution curve (MDC) along the constant energy cut indicated by the straight line below the MDC. The double peak pointed out by the vertical arrows results from the splitting of the outer band, as indicated by the red arrows. (**C**) A stack of MDCs extracted at different energies from the spectrum in (A). For clarity the MDC curves are offset successively. (**D**) The ARPES spectrum along Γ-K, the data was acquired using soft X-rays with $h\nu$ = 350 eV. The band splitting was observed using both VUV-light and soft X-rays, which provide compelling evidence that band splitting is an intrinsic feature of the bulk states rather than a k_z broadening effect.

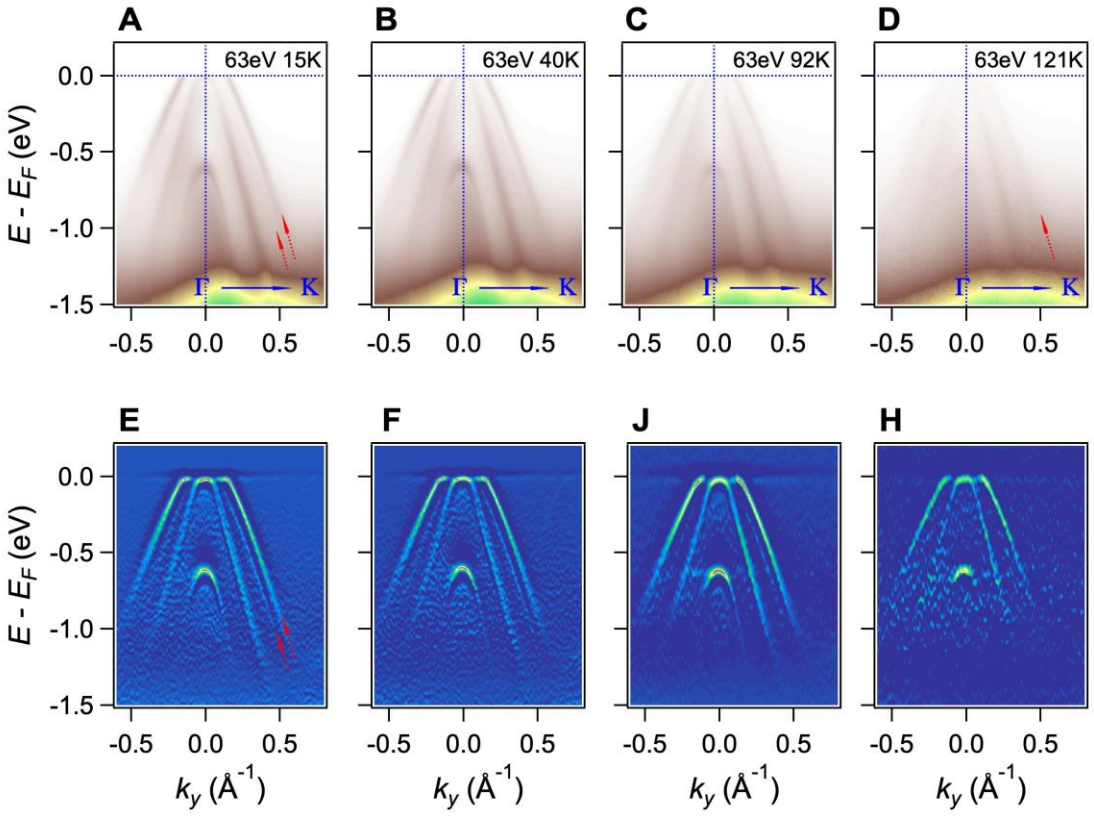

Fig. S2. Temperature effects on the band splitting in $EuCd_2Sb_2$. (**A** to **D**) The ARPES spectrum along Γ-K, as a function of temperature from 15 K to 121 K, recorded with *hv* = 63 eV. The two arrows in (A) indicate the band splitting at low temperature. Upon increasing the temperature, the split bands become blurred and are hard to distinguish above 100 K. (**E** to **H**) The curvature intensity plots of the spectra in (A to D).

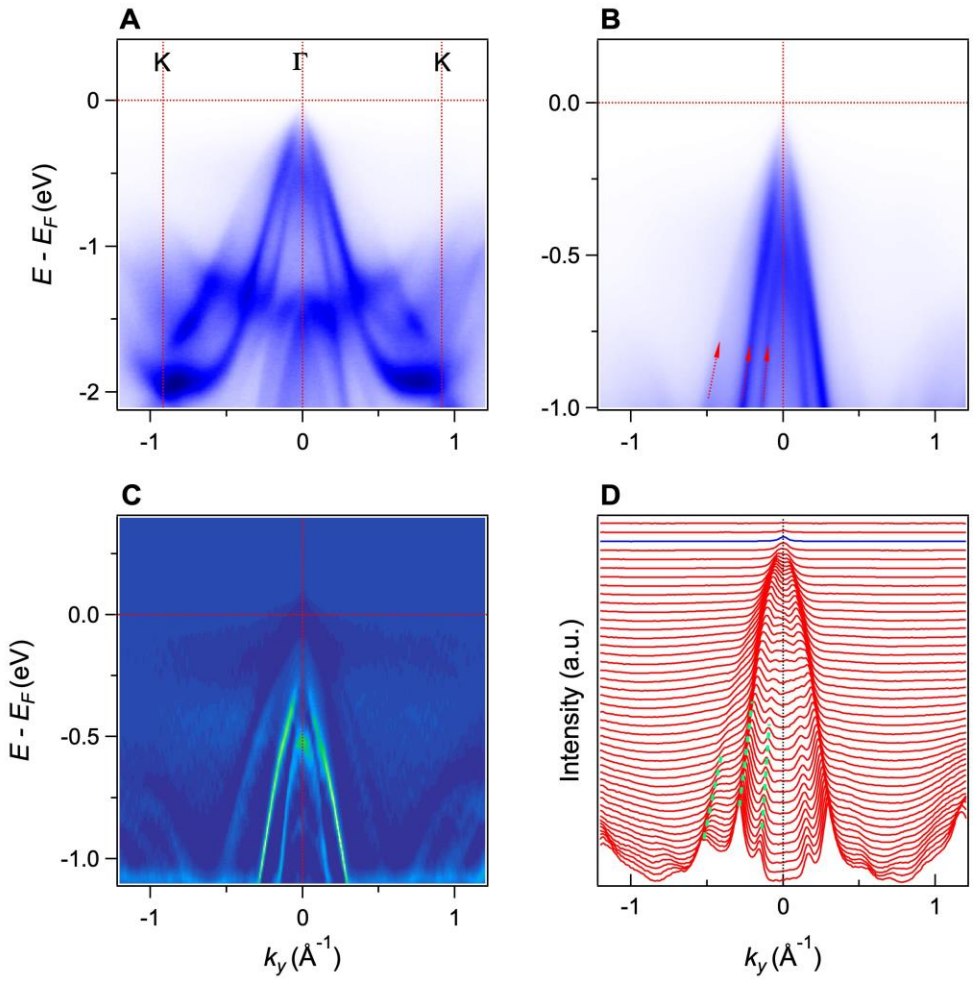

Fig. S3. Electronic structure of $BaCd_2As_2$. (**A**,**B**) The ARPES spectrum along K-Γ-K at two different energy scales. (**C**) Curvature intensity plot of the spectrum in (B). (**D**) A stack of MDCs extracted from the spectrum in (A) at different energies. For clarity the MDC curves are increasingly offset with increasing energy. The blue line indicates the Fermi level. No band splitting is observed in this non-magnetic compound, neither in the raw ARPES data nor in the curvature intensity plots or the MDC plots as indicated by the green dashed lines that trace the three doubly degenerate bands.

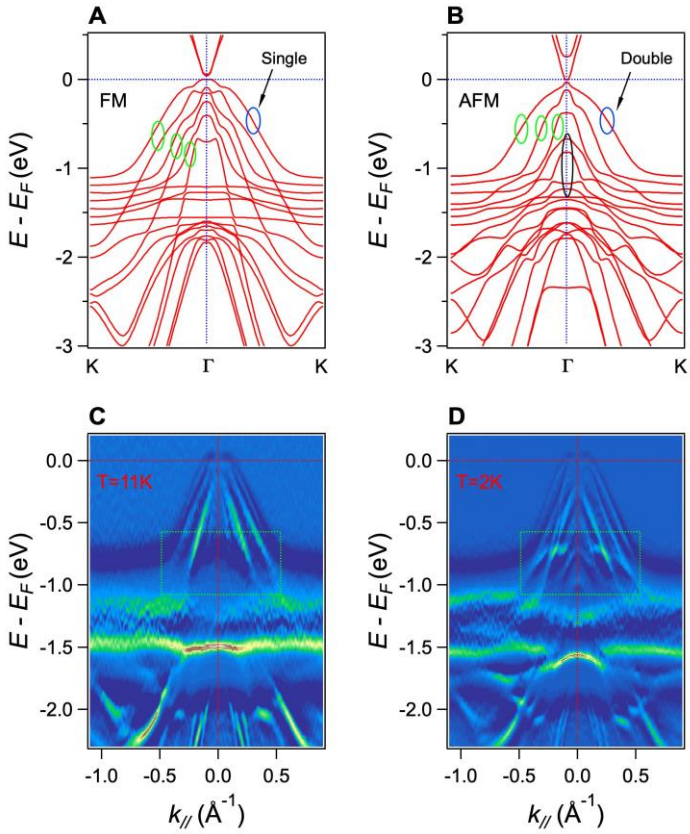

Fig. S4. Comparison of band structures below and above Néel temperature. (**A**) Calculated band structure along K-Γ-K in the FM phase. (**B**) Calculated band structure along K-Γ-K in the AFM phase. (**C**) Curvature intensity of band structure along cut0 as shown in Fig. 2A recorded at T=11K. (**D**) The same as C but recorded at T = 2 K. For the FM calculation shown in A, there are six singly degenerate As 4p bands near the Fermi level with their band top above -0.6 eV. These six bands organize into three spin-split pairs, as indicated with green ellipses. In the AFM calculation, shown in B, the six As 4p bands collapse into three bands indicated with green ellipses. Moreover, since the unit cell in the AFM phase is doubled along the z direction with respect to the FM phase, the BZ of the AFM is folded. The folding from the A point to the Γ point results in additional bands at Γ, as indicated by the black ellipse in B. It should be noted that, even though time reversal symmetry (*T*) is broken in the AFM phase, the double degeneracy of the bands is protected by the combination of parity symmetry (*P*), time reversal symmetry (*T*) and translation symmetry (*L*) by one unit along the z-axis. More details can be found in (*36*). The ARPES data in the PM phase agrees well with the FM band calculation, as we discuss in the main text. As we cool below the Néel temperature, we observe three hole-like bands near the Fermi level with their band top above -0.4 eV. Moreover, a few

shallow bands appear between -0.5 to -1.0 eV (region indicated by the green box) which we interpret as the folded bands discussed in the AFM calculation. These folded shallow bands cannot be observed in the PM phase above T_N.

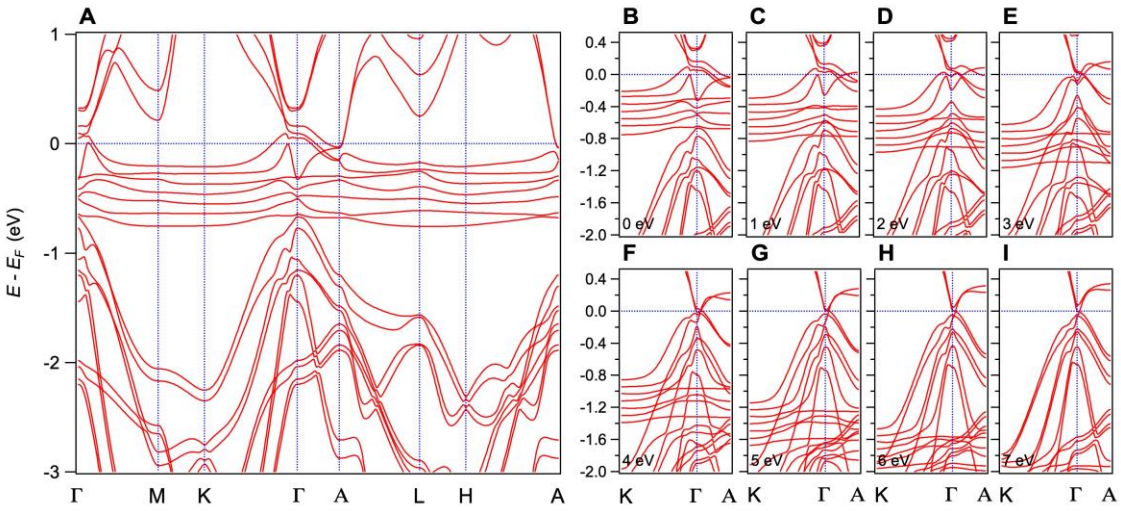

Fig. S5. Calculated band structures of $EuCd_2As_2$ with magnetic moments oriented along the *c* axis, as a function of onsite Coulomb interaction *U*. (**A**) Band dispersions along high-symmetry lines, calculated with U = 0 eV. (**B** to **I**) bands along K-Γ-A with U values from 0 to 7 eV.

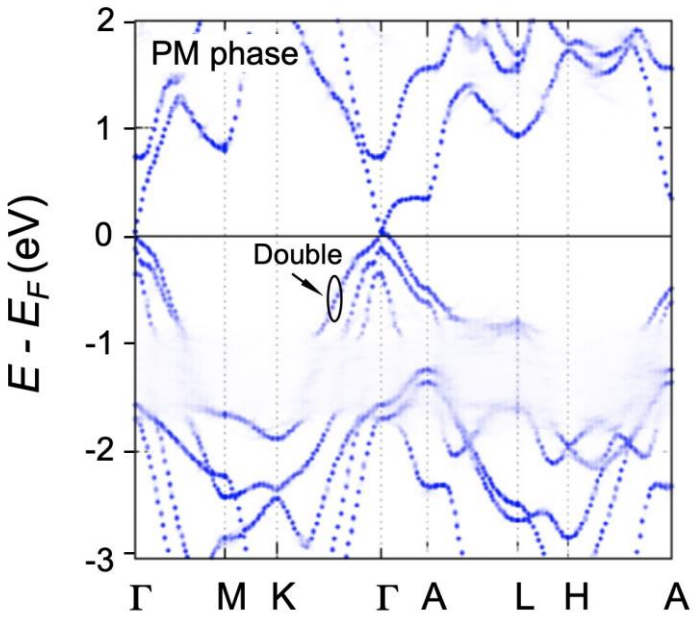

Fig. S6. Calculated band structure of $EuCd_2As_2$ along high-symmetry lines, deeply within the PM phase. Here, we set random directions for the Eu magnetic moments in a 4 by 4 by 1 enlarged unit cell (with a negligible average magnetization) in order to describe slow, but uncorrelated magnetic fluctuations. The results are unfolded to the single-formula-unit primitive cell. The six previously spin-split As 4p bands essentially collapse into three hole-like bands, as indicated in the figure for one of the three bands, and no discernible spin splitting is observed.

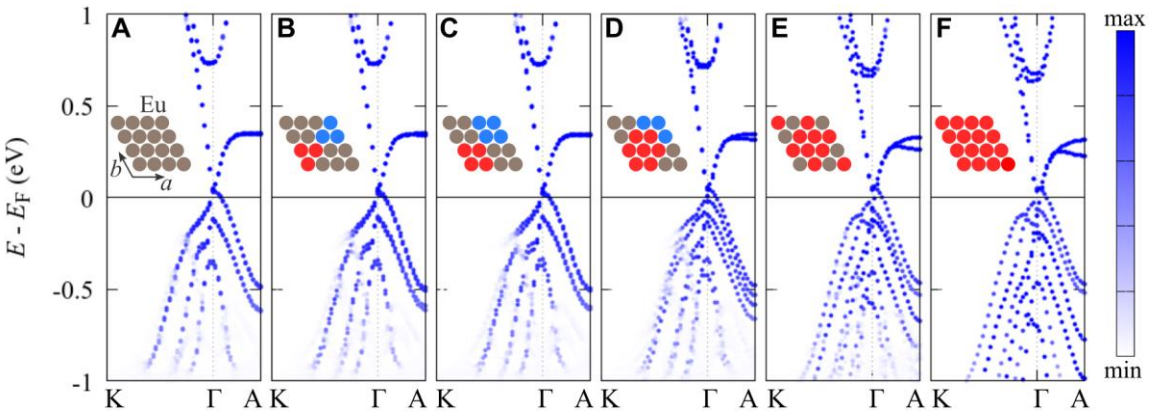

Fig. S7. Band structures with different magnetic backgrounds differing in size of FM clusters. Here, we consider an enlarged unit cell with different magnetic backgrounds, that differ in their average magnetization and clustering properties (or correlations): (**A**) Completely random spin configuration. (**B**) to (**E**) Structures containing small ferromagnetic clusters. (**F**) Ferromagnetic configuration. For each magnetic background we calculate the band structure along KΓA. We observe a spin splitting, which increases with the size of the included ferromagnetic clusters, and/or magnetization. However, to compare with the setting of an ARPES experiment, one should generate all possible magnetic structures, weighted with the Boltzmann weight of the associated spin patterns and average the resulting spectra. As explained in the main text, we expect this average to wash out the spin splitting of the bands, unless the correlation length is larger than the inverse of W_s. More details please see following discussion part.

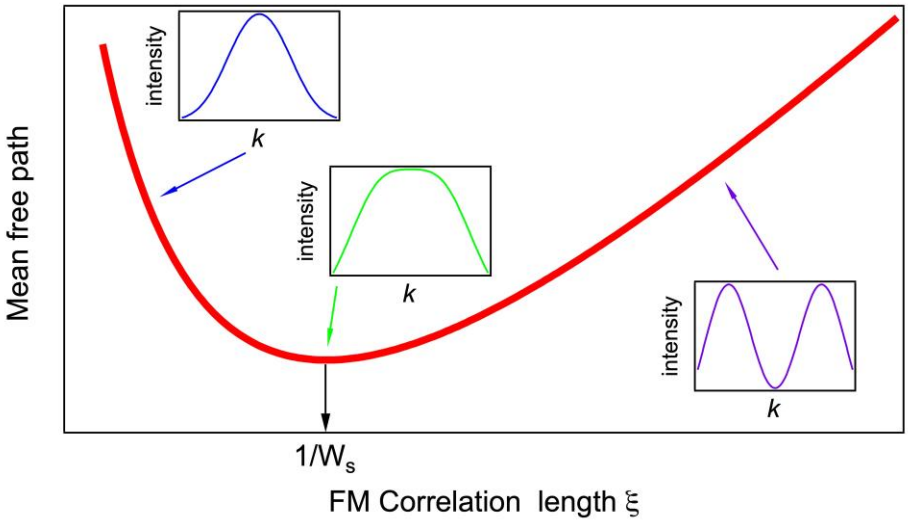

Fig. S8. The mean free path as a function of the FM correlation length.

Table S1. Positions of the Weyl points in $EuCd_2As_2$ depending on the spin orientation. θ is the angle between the spin orientation and the *c*-axis. φ is the angle between the projection of the spin orientation onto the *a*-*b* plane and the *b* axis.

θ	φ = 0°, Weyl point position: k_x (Å^{-1}), k_y (Å^{-1}), k_z (Å^{-1}))
0°	(0.0000, 0.0000, 0.0438), (0.0000, 0.0000, -0.0438)
30°	(0.0001, 0.0001, 0.0423), (0.0000, -0.0001, -0.0423)
45°	(0.0000, 0.00015, 0.0414), (0.0000, -0.00015, -0.0414)
60°	(0.0000, 0.00018, 0.0401), (0.0000, -0.00018, -0.0401)
75°	(0.0000, 0.0002, 0.0386), (0.0000, -0.0002, -0.0386)
90°	(-0.00008, -0.00015, 0.0335), (0.00008, 0.00015, -0.0335)
θ	φ = 90°
30°	(0.00016, 0.00004, 0.0423), (-0.00016, -0.00004, -0.0423)
45°	(0.00026, 0.00009, 0.0408), (-0.00026, -0.00009, -0.0408)
60°	(0.00037, 0.00016, 0.0394), (-0.00037, -0.00016, -0.0394)
75°	(0.00048, 0.00023, 0.0374), (-0.00048, -0.00023, -0.0374)
90°	(0.00014, 0.0007, 0.0316), (-0.00014, -0.0007, -0.0316)
θ	φ = 45°
30°	(0.00016, 0.00011, 0.0423), (-0.00016, -0.000011, -0.0423)
45°	(0.00029, 0.00018, 0.0408), (-0.00029, -0.00018, -0.0408)
60°	(0.00043, 0.00024, 0.0394), (-0.00043, -0.00024, -0.0394)
75°	(0.00058, 0.00033, 0.0374), (-0.00058, -0.00033, -0.0374)
90°	(0.00011, 0.0002, 0.0330), (-0.00011, -0.0002, -0.0330)